

Supplementary Information

1. Mathematical expressions of the functions in Section 2.1

1.1 Hanning function:

$$h(t) = \begin{cases} 0.5 + 0.5\cos(2\pi t) & |t| < \frac{1}{2}\tau \\ 0 & \text{otherwise} \end{cases} \quad \text{Eq.S1}$$

Its Fourier response:

$$H(f) = \tau \text{sinc}(\tau f) \cdot \frac{1}{2(1 - \tau^2 f^2)}$$

$$f = \gamma G_{\max} \cdot z \quad \text{Eq.S2}$$

$$H(z) = \tau \text{sinc}(\tau \gamma G_{\max} z) \cdot \frac{1}{2(1 - \tau^2 (\gamma G_{\max} z)^2)}$$

τ is duration of the function, i.e., RF duration, G_{\max} is the gradient amplitude during Hanning function, and z is the slice position.

1.2 Temporal sampling function:

For the label condition:

$$x_{\text{la}}(t) = \sum_{n=-\infty}^{\infty} \delta(t - nT) \quad \text{Eq.S3}$$

Its Fourier response:

$$X_{\text{la}}(f) = \sum_{n=-\infty}^{\infty} \delta(f - n\frac{1}{T})$$

$$f = \gamma G_{\text{ave}} z \quad \text{Eq.S4}$$

$$X_{\text{la}}(f) = \sum_{n=-\infty}^{\infty} \delta(\gamma G_{\text{ave}} z - n\frac{1}{T})$$

For the control condition:

$$x_{\text{con}}(t) = \sum_{n=-\infty}^{\infty} (\delta(t - 2nT) - \delta(t - (2n + 1)T)) \quad \text{Eq.S5}$$

Its Fourier response:

$$X_{\text{con}}(f) = \sum_{n=-\infty}^{\infty} \delta(f - \frac{1}{2T} - n\frac{1}{T})$$

$$f = \gamma G_{\text{ave}} z \quad \text{Eq.S6}$$

$$X_{\text{con}}(f) = \sum_{n=-\infty}^{\infty} \delta(\gamma G_{\text{ave}} z - \frac{1}{2T} - n\frac{1}{T})$$

T is the duration of a cycle in pCASL labeling, i.e., RF spacing, G_{ave} is the average gradient amplitude in a cycle of pCASL labeling.

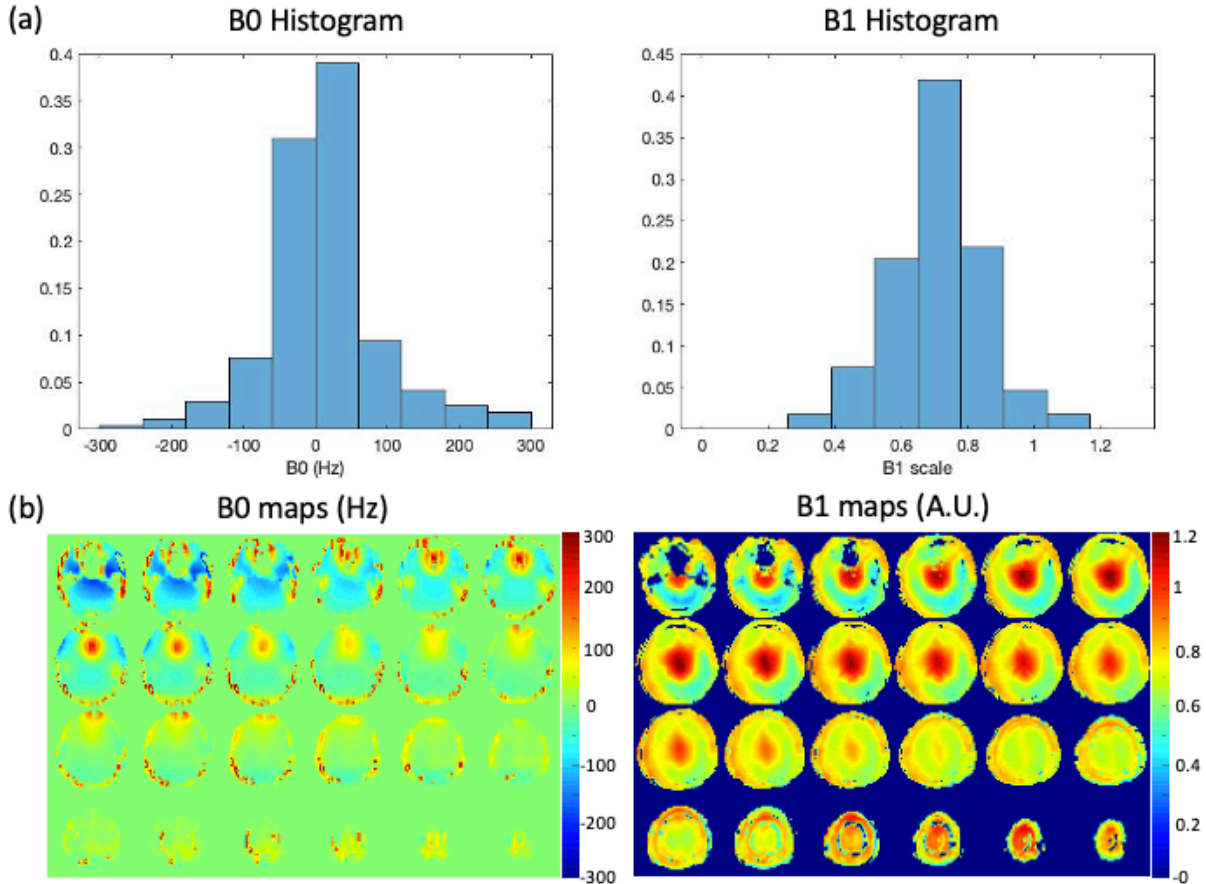
1.3 Fourier response of pCASL labeling:

$$H(z) = \hat{f}(h(t) \otimes x(t)) = H(z)X(z) \quad \text{Eq.S7}$$

1 \hat{f} represents Fourier transform.

2 **2. The subject cohort for B1 and B0 maps in the imaging volume**

3 This cohort included nine healthy subjects, and the B_1^+/B_0 maps of the pCASL imaging volume
4 were acquired with vendor adjustment scans and exported from system files (AdjDataUser.mat
5 and SysDataUser.mat). B1(CP mode) and B0 simming volumes were similar to the pCASL
6 scans. Figure S1 (a) shows the B0 and B1 histograms of this cohort, which supports our selection
7 of optimization ranges for BS (B1 scale: 0.35-1.15 and B0 offset: ± 250 Hz). Figure S1 (b) shows
8 the B0 and B1 maps of the pCASL imaging volume from a representative subject.



9
10 **Figure S1.** (a) B0 and B1 histogram from the cohort of nine subjects. (b) B0 and B1 maps from a
11 representative subject.

12 **3. Optimized BS Pulse definition and parameters**

13
14 HS pulse

$$\begin{aligned} |B_1(t)| &= \text{Sech}(\beta t) \\ \Delta\omega(t) &= -\mu\beta \tanh(\beta t) \end{aligned} \quad \text{Eq.S8}$$

17

1 WURST pulse

$$|B_1(t)| = 1 - |\sin(\frac{\pi}{2}t)|^n$$

$$\Delta\omega(t) = kt$$

Eq.S9

4 MATPULSE has a fixed shape that was defined within the software [1]. Only duration and
5 amplitude of the pulse were adjusted in the optimization.

6 **Table S1.** BS pulse parameters

	DURATION (MS)	PEAK AMPLITUDE(μ T)	PULSE- SPECIFIC	RELATIVE SAR
3T PULSE (MATPULSE)	10.24	10	/	1
OPTIM	6	20	/	4.7
HS	12	20	$\mu=600, \beta=4.4$	2.3
WURST	11	20	$n=2.5, k=650$	3.7
MATPULSE	9	20	/	3.1

7

8 **4. Theoretical formulation of OPTIM**

9 The RF pulse OPTIM is designed by means of ensemble-based time optimal control [2]. Key
10 component is definition of a robust cost functional for the RF $B_1^+(t) = r(t) \cdot e^{i\varphi(t)}$ with $r(t) =$
11 $abs(B_1(t))$ and $\varphi = angle(B_1(t))$ as

12

$$13 \min_{r, \varphi, T_p} J = T_p + \frac{\alpha}{2} \sum_{i=0}^{N_u} r_i^2 + \frac{\alpha}{2} \sum_{i=0}^{N_u} \varphi_i^2 + \frac{\beta}{p} \sum_{i=1}^{N_{B_1}} \sum_{j=1}^{N_{\Delta B_0}} \left(\frac{M_{i,j}(T_p) - (-1)}{\varepsilon} \right)^p \quad \text{Eq.S10}$$

14

15 with constraint

$$16 \begin{cases} \frac{dM_{i,j}(t)}{dt} = A_{i,j} \cdot M_{i,j}(t) + b, \\ M_{i,j}(0) = (0,0,1)^T, \forall i = 1, \dots, N_{B_1}, \forall j = 1, \dots, N_{\Delta B_0}, \forall t \in [0, T_p], \\ 0 \leq r(t) \leq r_{\max}, 0 \leq \varphi(t) < 2\pi. \end{cases} \quad \text{Eq.S11}$$

17

18 Therein, T_p is the pulse duration to be minimized, and $\alpha (>0)$ is the regularization parameter.

19 The last term within Eq.S10 ensures inversion efficiency of the z-component of the

20 magnetization $M_{i,j}$ (penalization parameter $\beta > 0$). Hereby, N_{B_1} discrete values of B_1^+ scales are

21 assumed, and $N_{\Delta B_0}$ different instances of B_0 offsets. The parameter ε defines the gap to the

22 desired magnetization, i.e. determines quality of the inversion within an L^p -norm, $p \geq 2$, p is even.

23 The Bloch equations Eq.S11 are solved for all instances i of B_1^+ scales, and offsets j of B_0 by

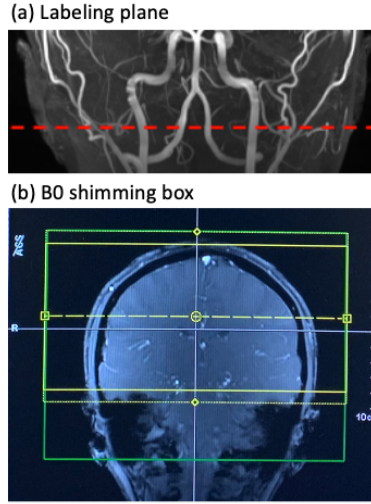
24 symmetric operator splitting [3]. Within the last row of Eq.S11, box constraints on the RF

25 magnitude and phase are defined.

26 The optimization itself is performed within a trust-region, semi-smooth quasi-Newton method

27 based on exact discrete derivatives supplied by adjoint calculus [4].

1 5. Labeling plane and B0 shimming



2

3 **Figure S2.** (a) Labeling plane was placed at the C1 segment (Bouthillier classification) of the
 4 internal carotid arteries. (b) B0 shimming box (green) covered the whole imaging volume with
 5 an extended bottom edge to cover labeling plane.

6 6. Calculation of IE map

7 Single slice 2D TFL sequences with and without a BS pulse were used to obtain IE maps of the
 8 BS pulses. The sequence with a readout immediately following one of BS pulses was employed
 9 to acquire the first image (S1). Then, a control sequence without the BS pulse was used to
 10 acquire the second image (S2). TR_{eff} was 10 s for both sequences to allow a full recovery of
 11 magnetization. The two images had the same FOV covering whole brain. An IE map can be
 12 obtained as $S1/S0$ with some additional scaling and intercept, which can be calculated as follows,

13

$$14 \quad S_{1/2} = \left| \left[M_{1/2} (E_1 \cos \theta)^{j-1} + (1 - E_1) \frac{1 - (E_1 \cos \theta)^{j-1}}{1 - E_1 \cos \theta} \right] E_2 \sin \theta \right| \quad \text{Eq. S12}$$

15 Let $K = (E_1 \cos \theta)^{j-1}$ and $P = (1 - E_1) \frac{1 - (E_1 \cos \theta)^{j-1}}{1 - E_1 \cos \theta}$, and assume $M_2 = 1$ and M_1 is negative

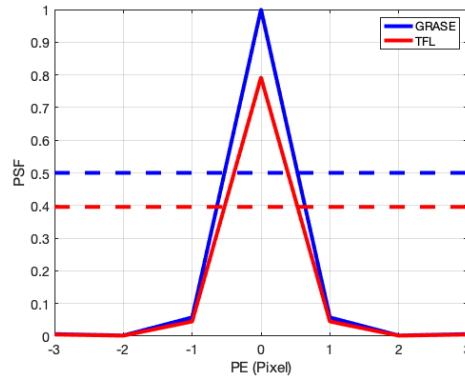
$$16 \quad \frac{S_1}{S_2} = \frac{M_1 K + P}{K + P} \quad \text{Eq. S14}$$

$$17 \quad IE = -M_1 = \frac{S_1}{S_2} \frac{K + P}{K} - \frac{P}{K} \quad \text{Eq. S15}$$

18 where Eq. S12 is based on [5], $E_1 = e^{-\frac{ES}{T_1}}$, $E_2 = e^{-\frac{TE}{T_2}}$, T_1 was set to 1500 ms, T_2 was set to 50
 19 ms, j was set to 16 for linear ordering, and FA θ was 8° . The experiment was repeated for axial,
 20 sagittal, and coronal views to evaluate all BS pulses.

1 7. Simulated PSFs in PE direction

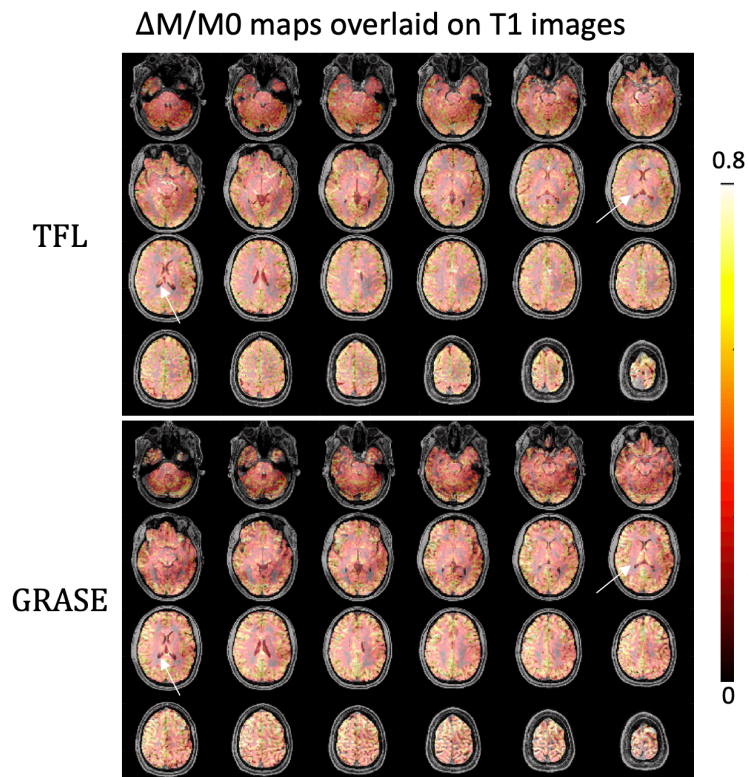
2 There was no significant difference of FWHM in PE direction between the two methods. FWHM
3 values were 1.06 and 1.08 for TFL-pCASL and GRASE-pCASL, respectively.



4
5 *Figure S3. Simulated PSFs of GRASE and TFL in PE direction.*

6

7 8. Coregistration of TFL- and GRASE-pCASL on T1



8
9 *Figure S4. T1 images were coregistered to the M0 images of TFL-pCASL and GRASE-pCASL*
10 *using SPM12, and $\Delta M/M_0$ maps overlaid on T1 images were shown. $\Delta M/M_0$ maps of TFL-*

1 *pCASL* matched perfectly with T1 images, whereas that of GRASE-*pCASL* showed some
2 distortions in bottom slices and frontal lobes. In addition, some detailed anatomical information
3 was less accurate in GRASE-*pCASL* compared to TFL-*pCASL*. As indicated by white arrows,
4 there was a slight shift of the hippocampus between GRASE-*pCASL* and T1 images.

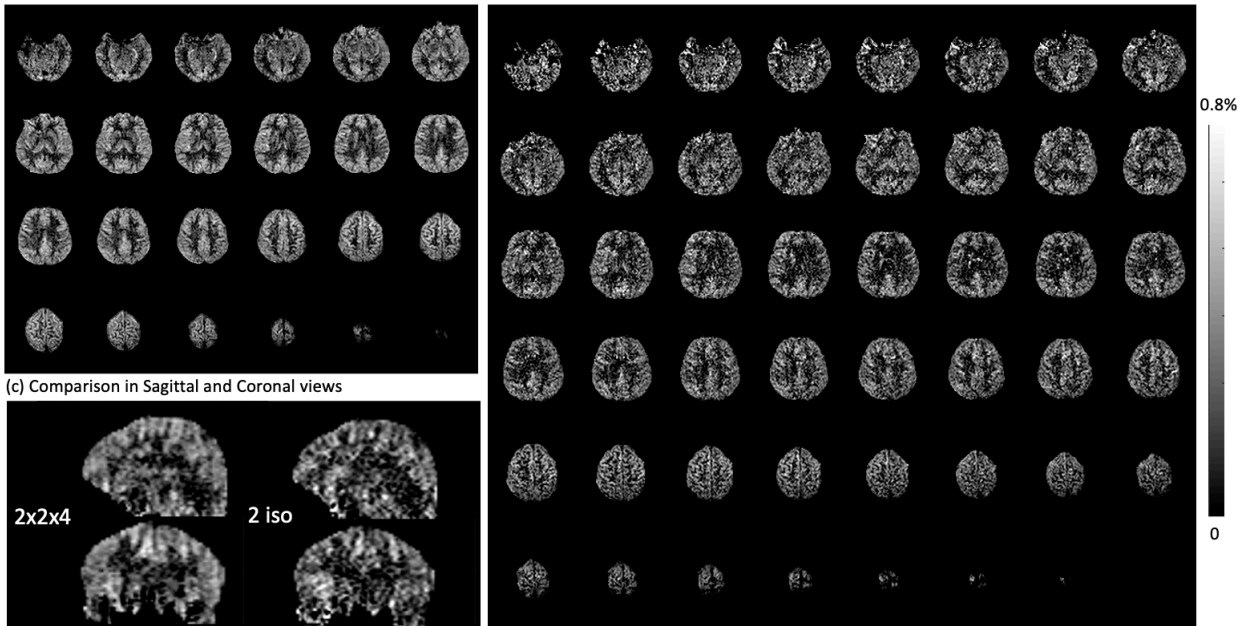
5 **9. Higher resolution (2 mm isotropic) protocol**

6 A 2 mm isotropic high-resolution protocol was tested with adjusted parameters, including
7 resolution = $2 \times 2 \times 2$ mm³, FOV = $224 \times 192 \times 104$ mm³, matrix size = $112 \times 96 \times 52$, 4 oversampled
8 slices, $N_{\text{seg}} = 4$, 26 measurements, including an M0 image, acquired in 12 min 10 s.

9 Figure S5 (a) and (b) display $\Delta M/M0$ maps with a standard $2 \times 2 \times 4$ mm resolution and a 2 mm
10 isotropic high resolution, respectively. In Fig. S5 (c), higher resolution revealed finer through-
11 plane details and more accurate delineation of GM/WM boundaries than standard resolution.
12 However, SNR was lower with the finer resolution.

(a) $\Delta M/M0$ maps acquired with $2 \times 2 \times 4$ mm resolution

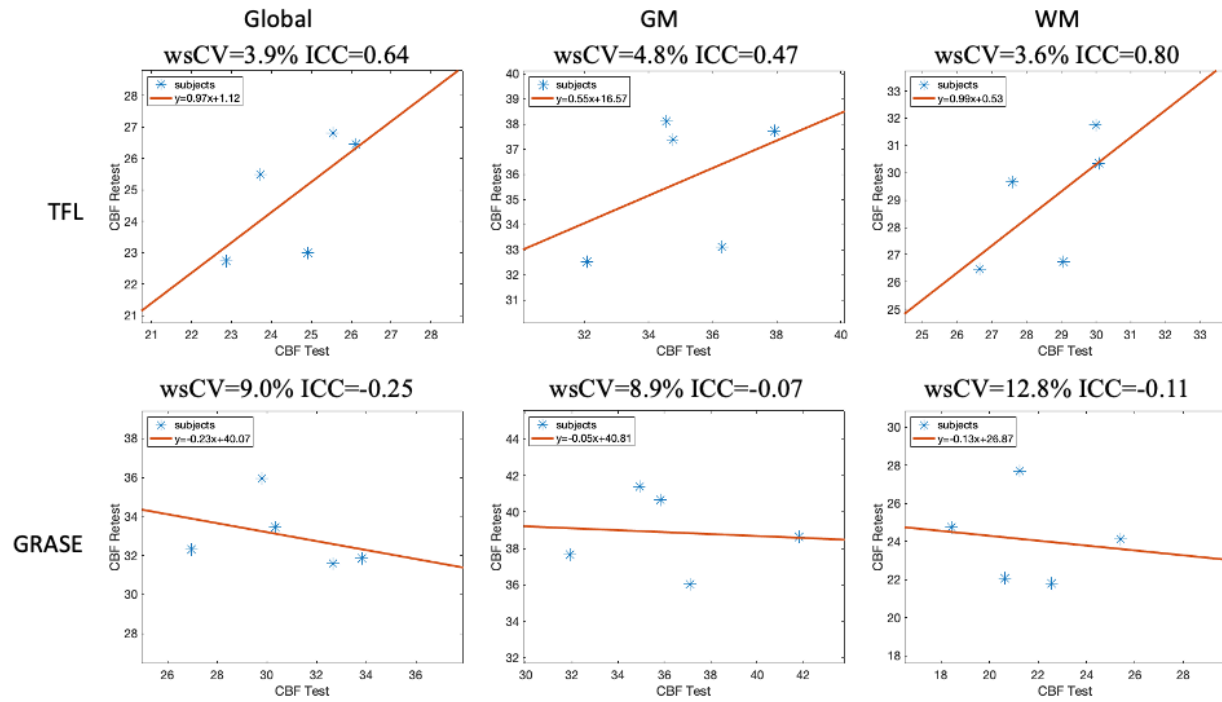
(b) $\Delta M/M0$ maps acquired with 2 mm isotropic resolution



13

14 **Figure S5.** (a) and (b) shows $\Delta M/M0$ maps acquired with $2 \times 2 \times 4$ mm³ and 2 mm isotropic
15 resolutions on the same subject. Anatomical details, such as orbitofrontal cortex, choroid plexus,
16 cerebellum, and gyri, can be discerned. (c) Comparison of the two scans in Sagittal and Coronal
17 views. Finer through-plane details can be observed with 2 mm isotropic resolution.

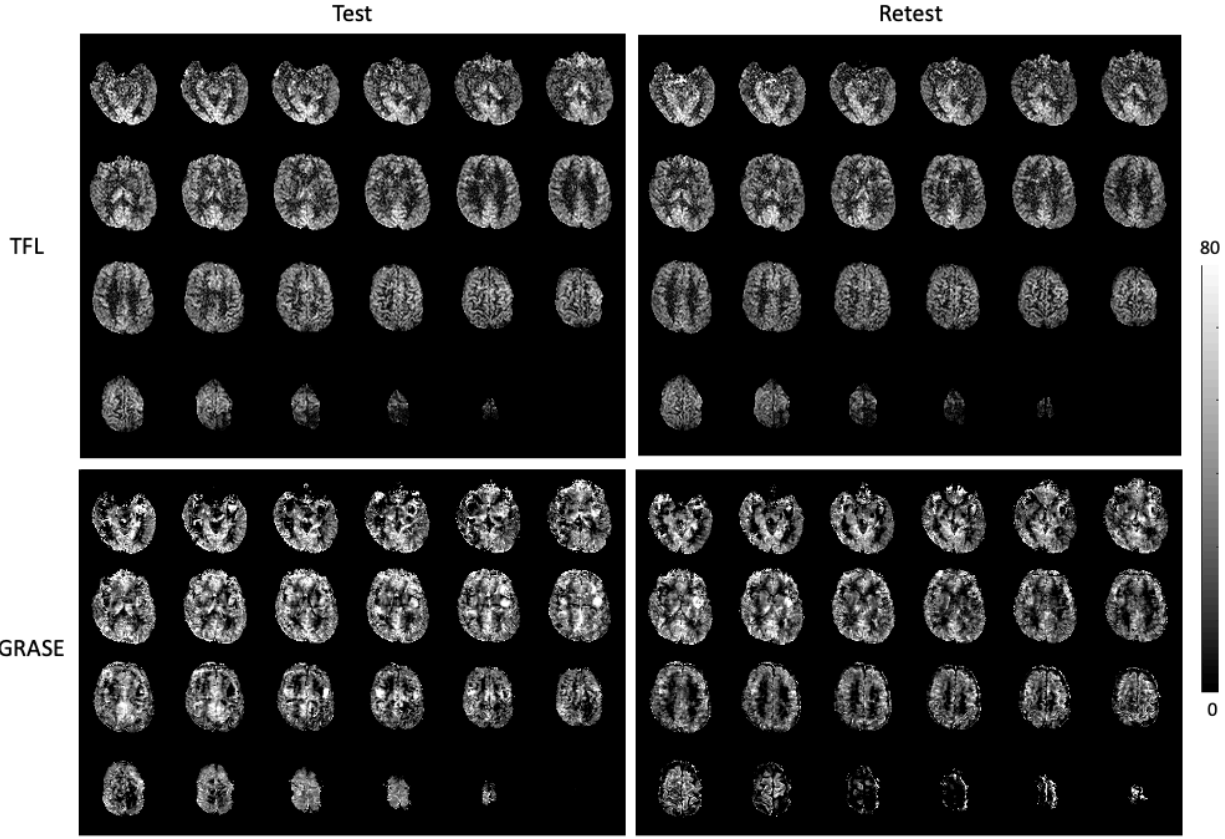
18 **10. Test-retest repeatability**



1

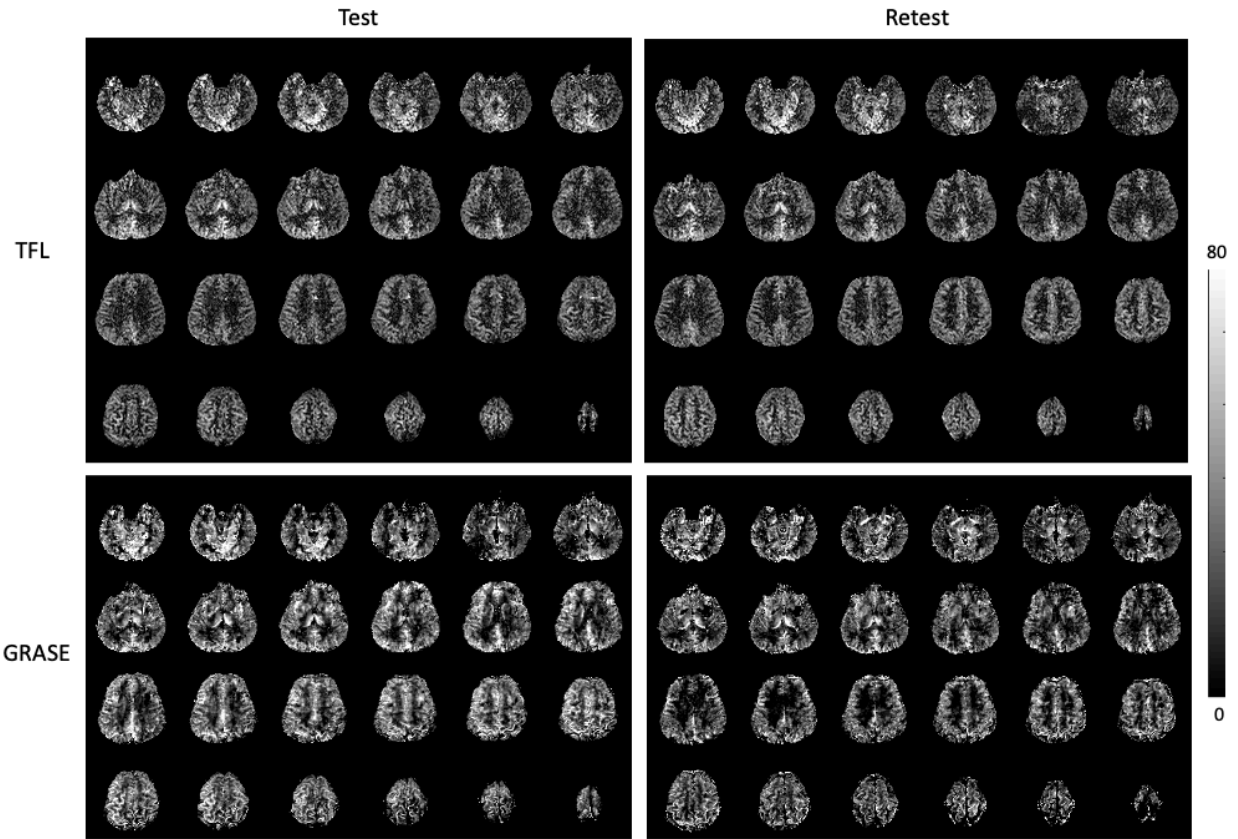
2 **Figure S6.** Scatter plots of test-retest results of TFL- and GRASE-pCASL. wsCV and ICC were

3 listed.



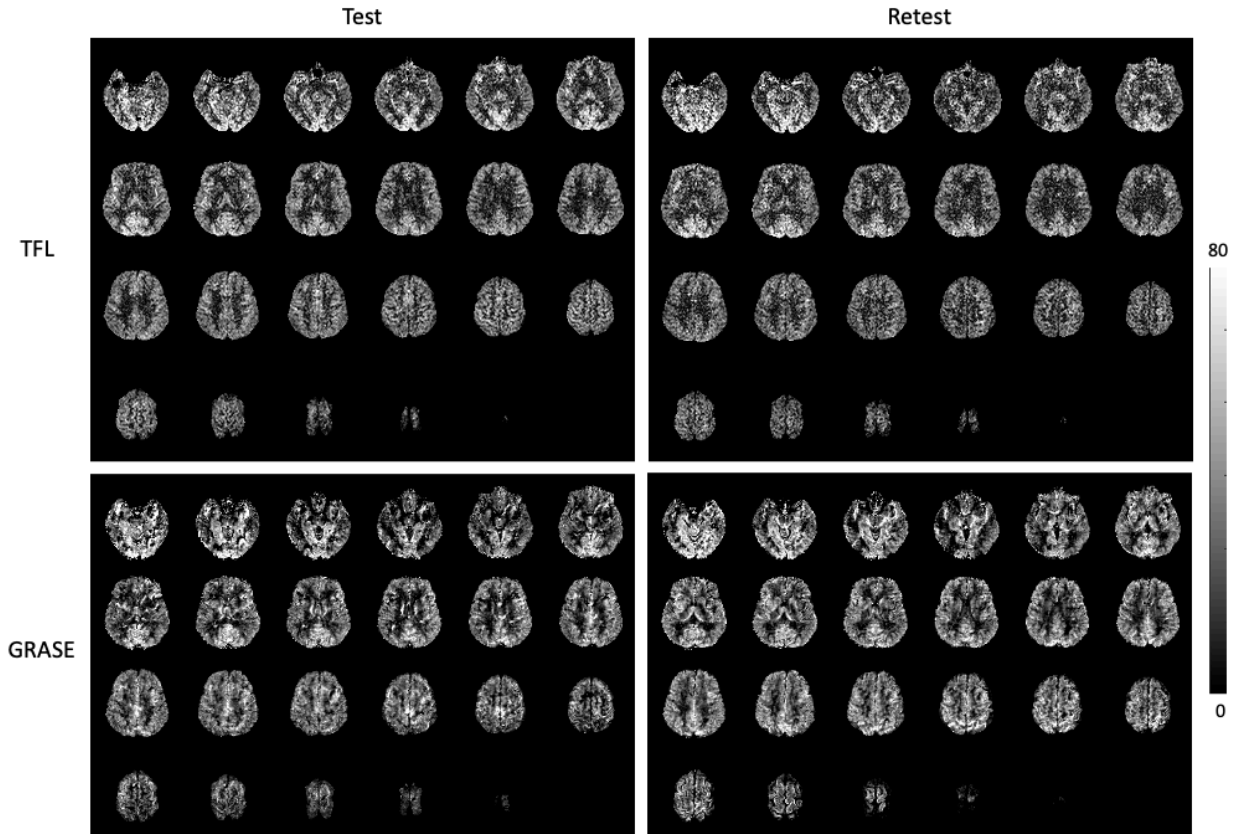
1

2 **Figure S7.** CBF (ml/100g/min) maps of subject 2 in two visits using TFL- and GRASE-pCASL.



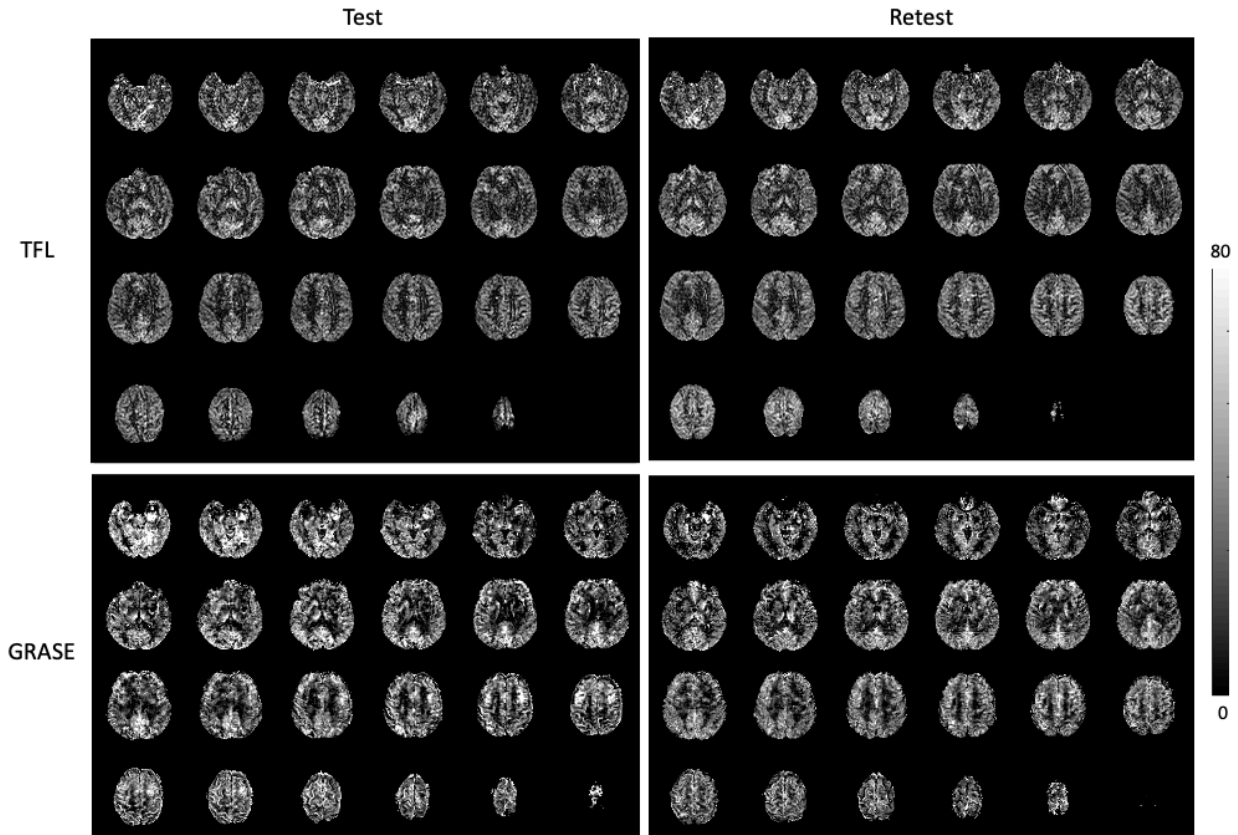
1

2 **Figure S8.** CBF (ml/100g/min) maps of subject 3 in two visits using TFL- and GRASE-pCASL.



1

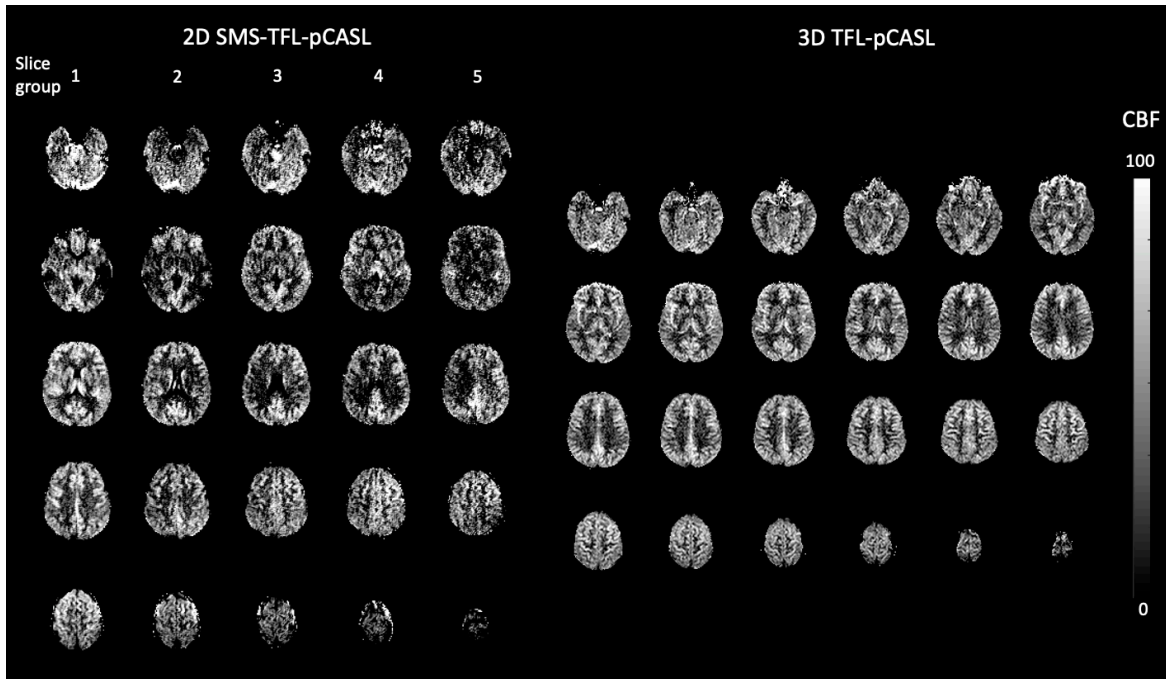
2 **Figure S9.** CBF (ml/100g/min) maps of subject 4 in two visits using TFL- and GRASE-pCASL.



1
2 **Figure S10.** CBF (ml/100g/min) maps of subject 5 in two visits using TFL- and GRASE-pCASL.

3 **11. CBF and SD maps of 2D SMS-pCASL**

4 CBF can be quantified for 2D SMS-pCASL based on Eq. 6 taking different PLDs (245 ms delay
5 between slice groups) for the 5 slice groups. In addition, j in Eq. 6 was set to 24 because k-space
6 center was acquired at the 24th excitation. Figure S11 compares CBF maps of a subject acquired
7 by 2D SMS-TFL-pCASL and 3D TFL-pCASL. Although intensity decay can be corrected for
8 later slice groups of SMS-TFL-pCASL, noisier appearance can be still observed.

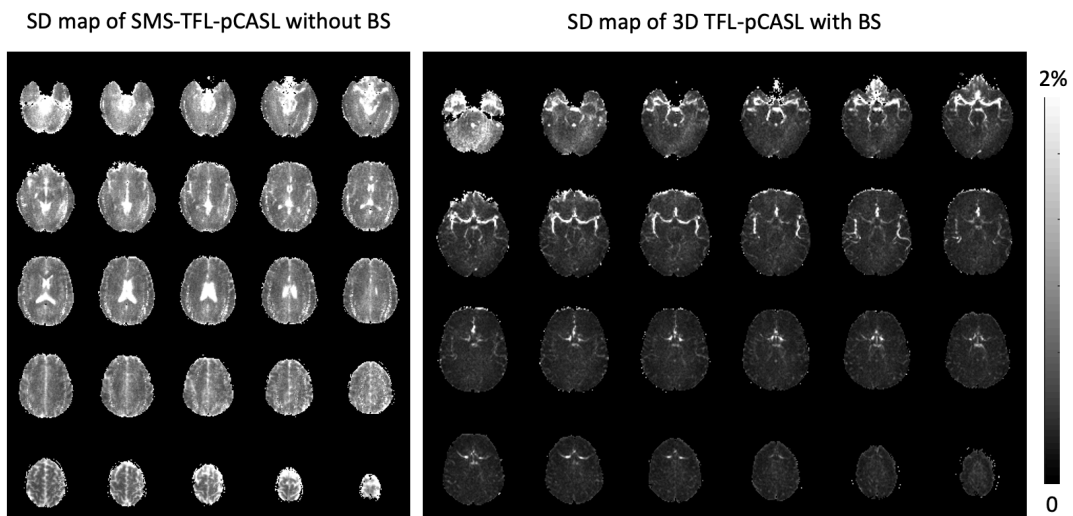


1

2 **Figure S11.** CBF (ml/100g/min) maps of 2D SMS-TFL-pCASL and 3D TFL-pCASL.

3 SNR of SMS-TFL-pCASL may also be further affected by reduced tSNR due to the lack of BS.
 4 tSNR values in the brain mask were 0.31 and 1.07 for SMS-TFL-pCASL and 3D TFL-pCASL,
 5 respectively. Figure S12 compares the temporal noise SD maps of perfusion images acquired
 6 with SMS-TFL-pCASL and 3D TFL-pCASL. Due to substantially higher intensity of the SD
 7 map of SMS-TFL-pCASL than its PWI, the intensity of two SD maps were scaled down by a
 8 factor of 10. Figure S12 shows overwhelming temporal noise from CSF and tissues for SMS-
 9 TFL-pCASL, while only some inflow vessel signal can be seen in 3D TFL-pCASL. The result
 10 may suggest that BS is also necessary for SMS-TFL-pCASL.

11

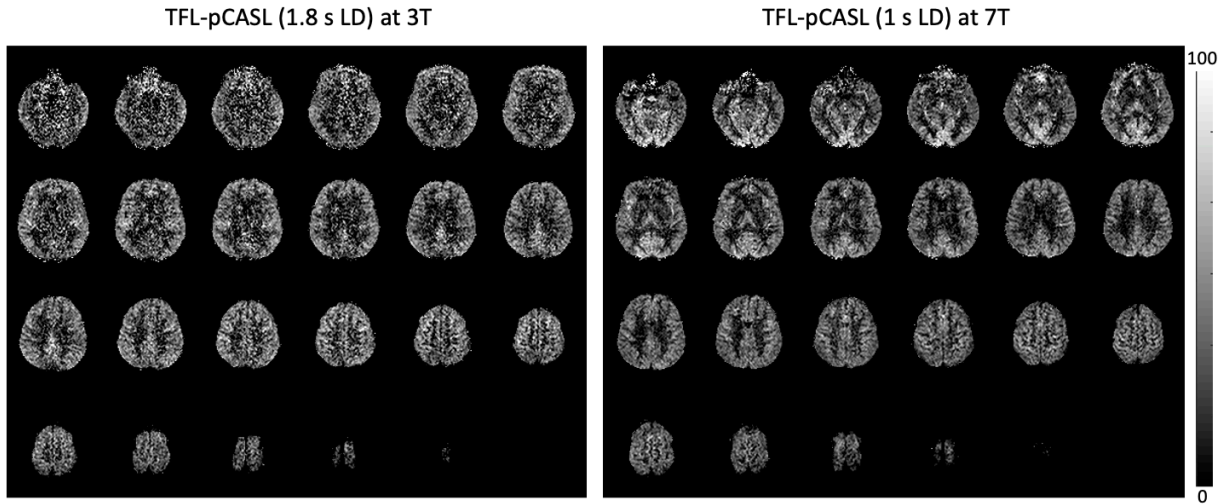


12

1 **Figure S12.** Temporal noise SD maps calculated from a series of individual $\Delta M/M_0$ maps
2 acquired by 2D SMS-TFL-pCASL without BS and 3D TFL-pCASL with BS.

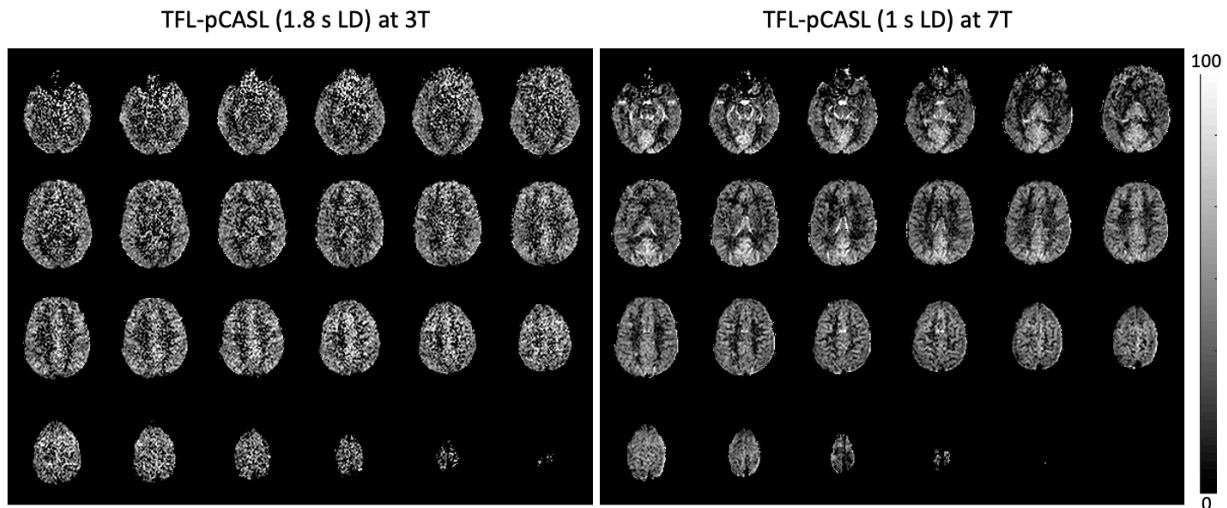
3

4 12. Comparison of 3T and 7T



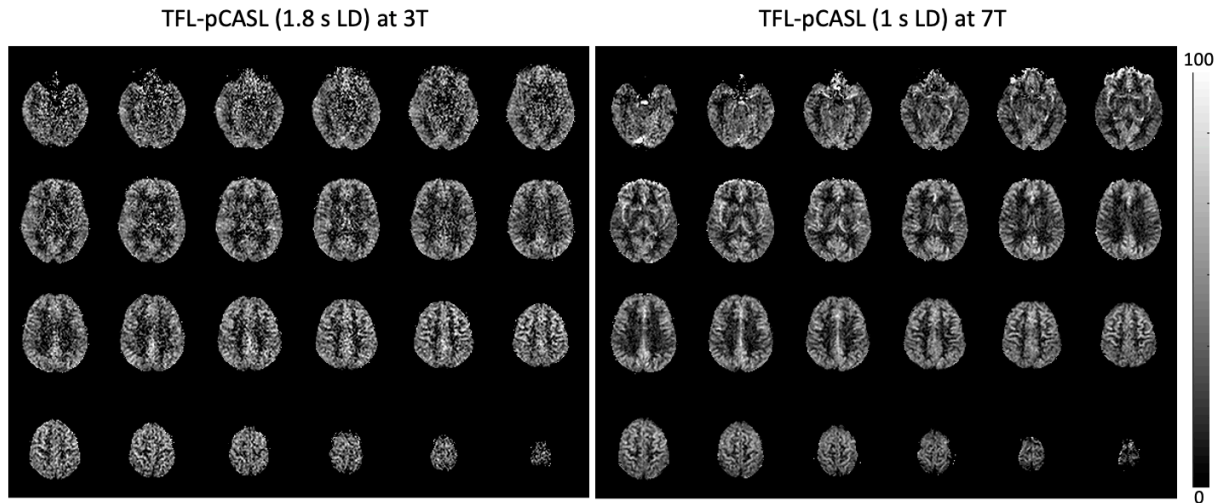
5

6 **Figure S13.** CBF (ml/100g/min) maps of subject 2 acquired by TFL-pCASL at 3T and 7T,
7 respectively. 3T ASL used 1.8 sec LD, while 7T ASL used 1 sec LD.

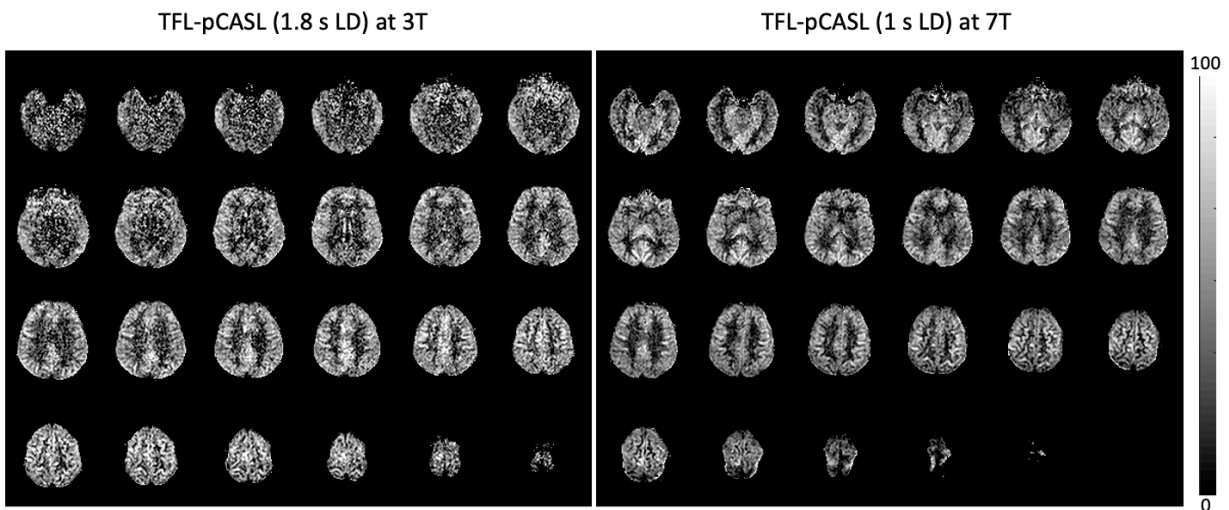


8

9 **Figure S14.** CBF (ml/100g/min) maps of subject 3 acquired by TFL-pCASL at 3T and 7T,
10 respectively. 3T ASL used 1.8 sec LD, while 7T ASL used 1 sec LD.

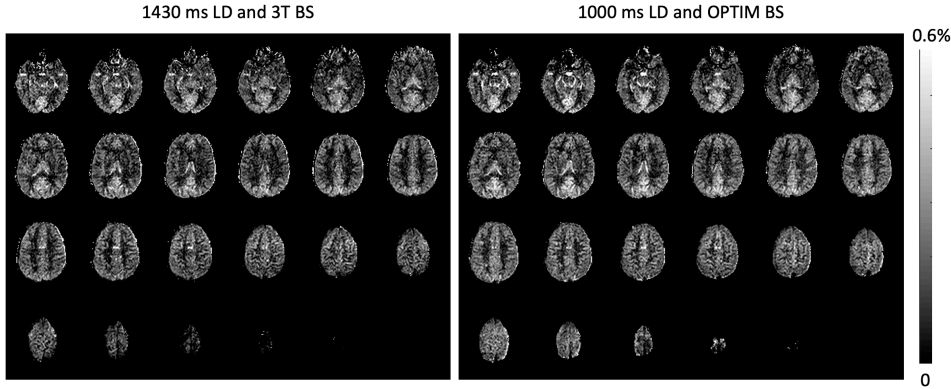


1
 2 **Figure S15.** CBF (ml/100g/min) maps of subject 4 acquired by TFL-pCASL at 3T and 7T,
 3 respectively. 3T ASL used 1.8 sec LD, while 7T ASL used 1 sec LD.



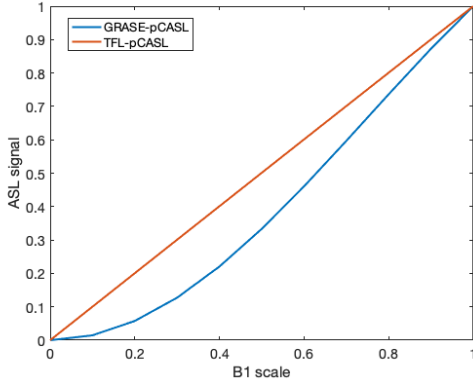
4
 5 **Figure S16.** CBF (ml/100g/min) maps of subject 4 acquired by TFL-pCASL at 3T and 7T,
 6 respectively. 3T ASL used 1.8 sec LD, while 7T ASL used 1 sec LD.

7 **13. Comparison of the default protocol and a protocol using 3T BS**
 8 **and 1430 ms LD**



1
 2 **Figure S17.** $\Delta M/M_0$ maps acquired with two protocols that used 1430 ms LD and 3T BS and
 3 1000 ms LD and OPTIM BS, respectively. The two protocols had the same SAR. The measured
 4 $\Delta M/M_0$ values in the GM mask were 0.19% and 0.21% for the former and the latter protocol,
 5 respectively.

6 **14. Simulation of ASL signal of TFL- and GRASE-pCASL under**
 7 **B1 inhomogeneity**

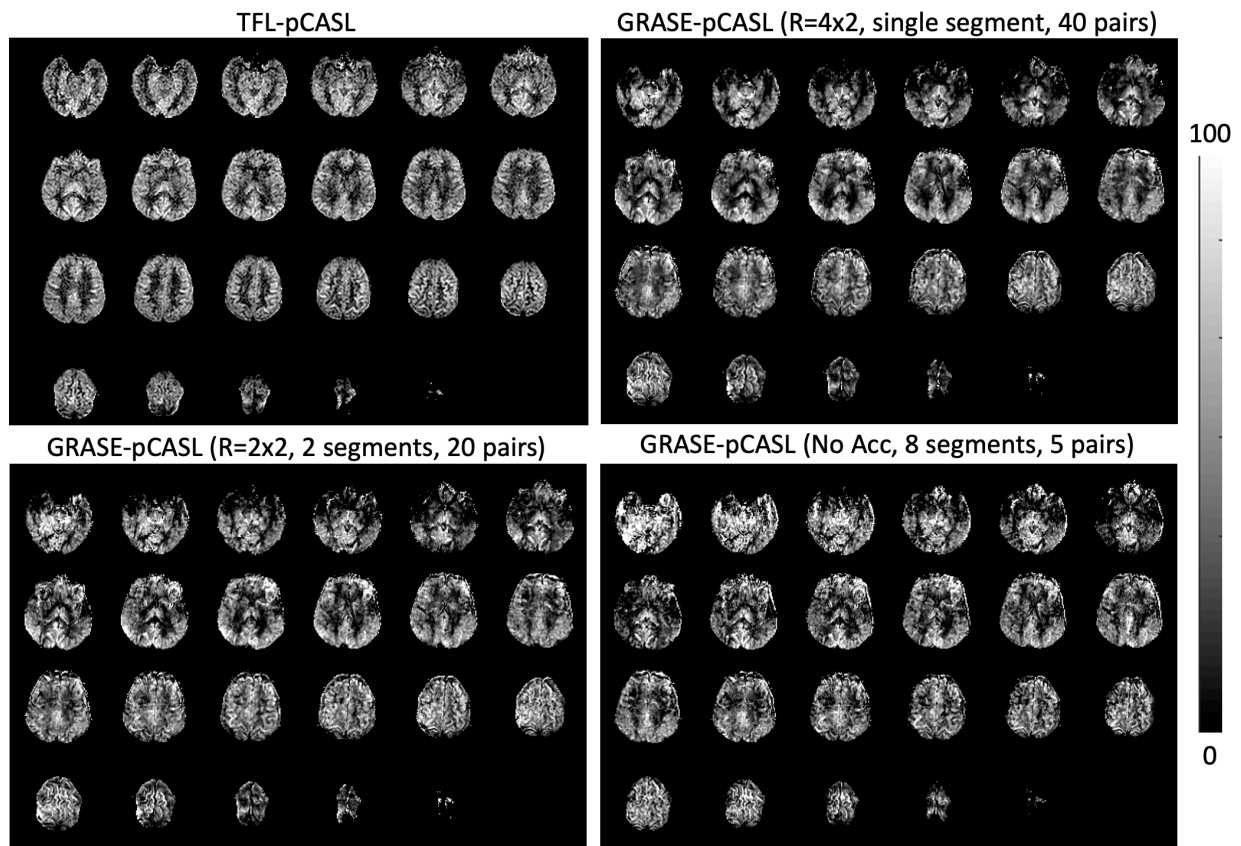


8
 9
 10 **Figure S18.** Relationships between ASL signal and B1 scale for TFL- and GRASE-pCASL that
 11 were simulated based on Eq. 4 and 5, respectively. For each sequence, signal intensities were
 12 normalized by the signal intensity that was obtained with the nominal FA (B1 scale = 1).

13 **15. GRASE-pCASL using same sampling pattern as TFL-pCASL**

14 In our comparison study, TFL- and GRASE-pCASL used different sampling patterns and
 15 reconstruction methods. We believe it is important to compare TFL-pCASL with the best
 16 available GRASE-pCASL option. The reason that we chose the single segment TGV
 17 reconstruction for GRASE-pCASL is that this setup is robust to physiological fluctuation
 18 between segments and is more SNR efficient than segmented TGV reconstruction and full-
 19 sampled inverse FFT reconstruction according to [6]. Also, the reason that we chose the
 20 undersampling pattern with $R=3 \times 3$ instead of $R=4 \times 2$ (identical to TFL-pCASL if two

1 control/label pairs were combined as segments) for GRASE-pCASL is that $R=3 \times 3$ significantly
 2 decreases the number of spin echoes from 14 to 10 with the cost of 4 ms longer TE compared to
 3 $R=4 \times 2$.
 4 Nevertheless, here we present the GRASE-pCASL CBF maps acquired with the $R=4 \times 2$
 5 undersampling and reconstructed with three reconstruction options, including single segment
 6 TGV reconstruction, two segments TGV reconstruction, and eight segments IFFT reconstruction.
 7 Imaging parameters were: resolution = $2.1 \times 2.1 \times 4 \text{ mm}^3$, FOV = $200 \times 200 \times 112 \text{ mm}^3$, matrix size
 8 = $112 \times 92 \times 28$, 6 oversampled slices, bandwidth = 2170 Hz/pixel, echo spacing = 0.53 ms, TE =
 9 18 ms, 2D-CAIPIRINHA with $R=4 \times 2$, EPI factor = 23, turbo factor = 14, single shot, FA=120°,
 10 TR = 8 s, 88 measurements, including an M0 image, were acquired in 11 min 40 s. Distortions in
 11 GRASE images were corrected by using a blip-reversed scan and TOPUP (details see
 12 supplement section 15).
 13

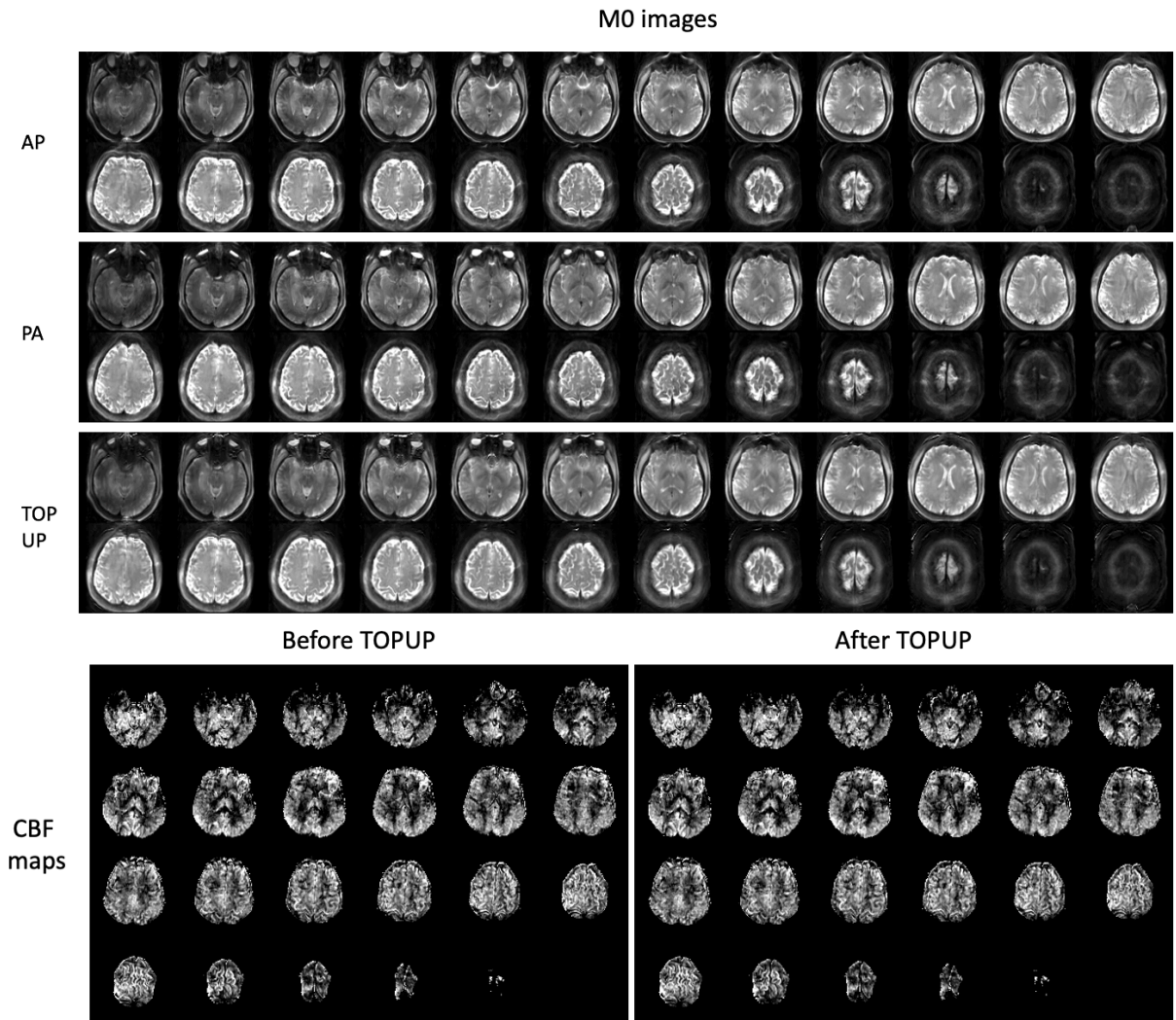


14
 15 **Figure S19.** CBF maps for a comparison of TFL-pCASL and GRASE-pCASL with $R=4 \times 2$ and
 16 three different reconstruction options, including single segments, two segments, and 8 segments.
 17

18 Figure S19 shows the comparison of the CBF maps acquired by TFL-pCASL and GRASE-
 19 pCASL with $R=4 \times 2$ and three different reconstruction options. Compared to TFL-pCASL, all
 20 GRASE-pCASL images showed artifacts and signal dropouts caused by susceptibility effects.
 21 Although similar image appearance was observed among GRASE-pCASL images reconstructed
 22 by three reconstruction options, the single segment image with TGV reconstruction showed the
 23 highest SNR. The global SNR values were measured as 2.41 for TFL-pCASL, and 3.82, 2.29,
 24 and 1.14 for GRASE-pCASL with 1, 2, and 8 segments, respectively.

1 16. Distortion correction for GRASE-pCASL

2 Distortion correction was attempted to improve the image quality of GRASE-pCASL that was
3 described in supplement section 14 (R=4x2, single segment). A separate blip-reversed scan with
4 PE direction of posterior to anterior (PA) was acquired, while the PE direction of GRASE-
5 pCASL scans was AP. The TOPUP function in FSL [7] was used to correct distortion with the
6 proper input parameters, such as blip directions and total readout time of 12.2 ms (defined as the
7 center of first EPI echo to the center of the last EPI echo).



8 **Figure S20.** Blip-reversed M0 images and the M0 images after distortion correction, and CBF
9 maps before and after TOPUP.

10 Figure S20 shows blip-reversed M0 images and the M0 images after distortion correction, and
11 CBF maps before and after TOPUP. Although TOPUP successfully corrected distortions, the
12 signal loss related to susceptibility effects was not restored, which was reflected in the CBF
13 maps. There was no apparent difference between the CBF maps before and after TOPUP.
14

1 Reference

- 2 [1] G. B. Matson, “An integrated program for amplitude-modulated RF pulse generation and re-
3 mapping with shaped gradients,” *Magn. Reson. Imaging*, vol. 12, no. 8, pp. 1205–1225,
4 1994, doi: 10.1016/0730-725x(94)90086-7.
- 5 [2] C. Graf, M. Soellradl, C. S. Aigner, A. Rund, and R. Stollberger, “Advanced design of MRI
6 inversion pulses for inhomogeneous field conditions by optimal control,” *NMR Biomed.*, vol.
7 35, no. 11, p. e4790, 2022, doi: 10.1002/nbm.4790.
- 8 [3] C. Graf, A. Rund, C. S. Aigner, and R. Stollberger, “Accuracy and performance analysis for
9 Bloch and Bloch-McConnell simulation methods,” *J. Magn. Reson.*, vol. 329, p. 107011,
10 Aug. 2021, doi: 10.1016/j.jmr.2021.107011.
- 11 [4] F. Mannel and A. Rund, “A hybrid semismooth quasi-Newton method for nonsmooth
12 optimal control with PDEs,” *Optim. Eng.*, vol. 22, no. 4, pp. 2087–2125, Dec. 2021, doi:
13 10.1007/s11081-020-09523-w.
- 14 [5] Z. Zuo, R. Wang, Y. Zhuo, R. Xue, K. S. S. Lawrence, and D. J. J. Wang, “Turbo-FLASH
15 Based Arterial Spin Labeled Perfusion MRI at 7 T,” *PLOS ONE*, vol. 8, no. 6, p. e66612,
16 Jun. 2013, doi: 10.1371/journal.pone.0066612.
- 17 [6] S. M. Spann *et al.*, “Robust single-shot acquisition of high resolution whole brain ASL
18 images by combining time-dependent 2D CAPIRINHA sampling with spatio-temporal TGV
19 reconstruction,” *NeuroImage*, vol. 206, p. 116337, Feb. 2020, doi:
20 10.1016/j.neuroimage.2019.116337.
- 21 [7] S. M. Smith *et al.*, “Advances in functional and structural MR image analysis and
22 implementation as FSL,” *NeuroImage*, vol. 23 Suppl 1, pp. S208-219, 2004, doi:
23 10.1016/j.neuroimage.2004.07.051.